Assembly of Metallacages into Soft Suprastructures with Dimensions of up to Micrometers and the Formation of Composite Materials

Yan Sun[*,†,‡], **Fengmin Zhang**[§], **Shaowei Jiang**[‖], **Zhifeng Wang**[§], **Ruidong Ni**[⊥], **Heng Wang**[⊥], **Weidong Zhou**[§], **Xiaopeng Li**[⊥], and **Peter J Stang**[*,‡]

[†]School of Chemistry and Chemical Engineering, Yangzhou University, Yangzhou, Jiangsu 225002, P. R. China

[‡]Department of Chemistry, University of Utah, 315 South 1400 East, Room 2020, Salt Lake City, Utah 84112, United States

[§]Testing Center of Yangzhou University, Yangzhou, Jiangsu 225002, P. R. China

[‖]School of Medicine, Shanghai Jiao Tong University, Shanghai 200240, P. R. China

[⊥]Department of Chemistry, University of South Florida, 4202 East Fowler Avenue, Tampa, Florida 33620, United States

Abstract

This work provides a platform for the rapid generation of superstructure assemblies with a wide range of lengths that can be used to access a variety of metal–organic complex-based soft superstructures. Metallacage-based microneedles that are nanometers in diameter and millimeters in length were generated in dichloromethane and ethyl acetate; their size could be controlled by adjusting the ratio of the two solvents. Interestingly, microflower structures could be formed by further assembly of the microneedles during solvent evaporation. Our study establishes a feasible method designed to broaden the range of suprastructures with emissions from blue and green to red through the co-assembly of lysine-modified perylene. Similar to the co-assembly of lysine-modified perylene with microflowers, chlorophyll-a and vitamin B_{12} were introduced into the microflowers during the assembly process, which may be exploited in studies of energy capture and nerve repair in the future
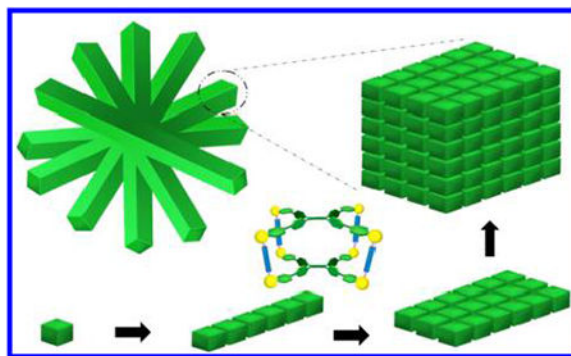
[*]**Corresponding Authors**: sunyan@yzu.edu.cn; stang@chem.utah.edu.

INTRODUCTION

From the formation of lipid bilayers[1] to molecular-level protein folding,[2] self-assembly occurs in nature in various forms.[3] A variety of natural structures can arise from repeated interactions between multiple copies of a single-molecular building block, endowing their hosts with enhanced functionalities and novel properties. Natural assemblies such as molecular motors,[4] enzymes,[5] viruses, and subcellular structures[6] often result from the self-limiting ordered oligomerization of multiple subunits.[7]

Thus, understanding self-assembly processes could give us a better understanding of life itself.[8] Inspired by natural assemblies, a wide variety of functional suprastructures, including micelles,[9] vesicles,[10] ribbons,[11] films,[12] fibers,[13] and tubes,[14] have been generated using small molecules,[15] macromolecules,[16] and polymers[17] as building blocks. Sophisticated designs and processes are usually needed to meet the required mechanical, electronic, optical, and magnetic properties.[18] Therefore, careful control of the various components is needed for preparing building blocks,[19] and not only the interactions mediating the dynamic self-assembly of the individual components but also the coexistence and communication of components of different types within larger, multicomponent ensembles must be considered. [20]

Coordination-driven self-assembly provides a bottom-up approach for constructing various functional metal–organic complexes (MOCs).[21] Furthermore, the dynamic nature of coordination bonds may also enable superstructure disassembly and subsequent reassembly with an external stimulus.[22] The modularity and simplicity of this method enable the transformation of different materials into modular "bricks" for constructing superstructures with increasing complexity and functionality, which have been used to construct novel switchable catalysts,[23] guest capture-and-release systems,[24] responsive soft materials,[25] and molecular mechanical actuators,[26] thus opening up routes toward rationally designed architectures.[27]

For example, Nitschke et al. used MOCs for selective anion extraction,[28] signal transduction, [29] the triggering of multiple structural transformations,[30] etc. Leigh et al. described a molecular machine that moves a substrate between different activating sites.[31,32] Anderson et al. reported the template-directed synthesis of a porphyrin nanoball.[33] Fujita et al. prepared palladium metal complexes and used them as catalyst carriers.[34] Most of these

MOCs have dimensions of only several nanometers, and investigations of these structures rely on the characterization of their crystal structure. However, most of the functional suprastructures in living organism have dimensions ranging from micrometers to centimeters and have forms of soft materials (whose structures are difficult to characterize by single-crystal diffraction).

A variety of species with diverse dimensions, including nanospheres,[35] nanodiamonds,[36] nanorods,[37] nanofibers,[38] membranes,[39] films,[40] and gels,[41] have been generated by the use of metallacycles[42] and metallacages[43] as building blocks.[44] These stimuli-responsive materials[45] have been used for light emission,[46] cell imaging,[47] heparin detection,[48] antitumor activity,[49] etc. However, almost all of these soft suprastructures were formed from metallacycles,[50] and the resultant structures are supramolecular network polymers.[51,52] Despite the tremendous progress made in the design of MOC-based supramolecular materials, it still remains a challenge to obtain uniform structures with designed size and shape. Thus, considerable effort has been made to prepare MOC-based hierarchical suprastructures. For example, van der Boom et al. reported the synthesis of diverse metal–organic (sub)-microstructures with a high degree of uniformity.[53,54] To the best of our knowledge, metallacage-based suprastructures with one-dimensional architectures and dimensions up to the micrometer scale remain rare.[55]

Here, we aim to develop an understanding of the formation of MOC (metallacage)-based soft suprastructures. Metallacages were synthesized using tetra(4-pyridylphenyl)ethylene (TPPE), dicarboxylate moieties, and *cis*-$(PEt_3)_2Pt(OTf)_2$. In order to minimize the impact of substituents on the assembly, dicarboxylate ligands without substituents were used as pillars, and the as-prepared metallacage was used as a model cage (cage **1**). By investigating the interactions between cage **1** with ethyl acetate, we were able to form microneedles with controllable sizes and emission from blue to green. In order to broaden the emission range, lysine-modified perylene[56] was then selected as the co-assembly component, and a similar suprastructure of perylene-containing aggregates was synthesized. The emission of these needles can be shifted from blue-green to blue-green-red by the co-assembly of lysine-modified perylene. Furthermore, hybrid materials could be obtained by the co-assembly of a fat-soluble biomolecule (chlorophyll-a) and a water-soluble biomolecule (vitamin B_{12}) with the microneedles.

RESULTS AND DISCUSSION

Cage **1** (Scheme 1) was prepared in acetone/water according to published procedures[46] and was identified by $^{31}P\{^{1}H\}$ NMR (Figure S1), ^{1}H NMR (Figure S2), and electrospray ionization time-of-flight mass spectrometry (ESI-TOF-MS) data (Figure S3). Solvent properties can strongly affect self-assembly behaviors as well as the assembled nanostructures. It is found that cage **1** dissolves well in dichloromethane (DCM) without forming observable aggregates but is insoluble in ethyl acetate (EA), likely due to the solvent polarity of EA. We thus chose DCM as a good solvent and EA as a poor solvent, and the self-assembly was induced via a so-called "phase-transfer" strategy.[16] Cage **1** was initially dissolved in DCM, and the prescribed amount of EA was added to give 10 μM solutions with different DCM/EA ratios. As shown in Figure S4, cage **1** displays two

characteristic absorptions at 282 and 336 nm in pure DCM. In pure EA, cage **1** displays a characteristic absorption at 330 nm (Figure S5). Upon addition of EA to give an 80% EA solution, the UV–vis spectrum showed a noticeable blueshift, suggesting conversion of the monomers into supramolecular assemblies (Figures S6). Similar EA-induced self-assemblies of cage **1** in DCM were further supported by fluorescence characterization (Figures S7–S9). Figure S9 presents the fluorescence spectrum of **1** at an EA content of 80% after 10 min. The peaks at 545 nm (DCM) and at 495 nm (EA) disappear, while a new peak at 450 nm appears. At the same time, a turbid solution could be observed at the interphase between the DCM and EA, demonstrating the formation of cage **1**-based aggregates. These newly formed aggregates were extracted from the DCM/EA interface and then examined by scanning electron microscopy (SEM). The images over a large area revealed that cage **1** can form ordered nanostructures in a DCM/EA mixture containing 80% EA. As shown in Figure 1a, numerous flower-like clusters can be observed. Magnification (Figure 1b) suggests that these flower-like clusters are composed of needle-like units. A further magnification of the image in Figure 1b shows that some overlap occurs among the microflowers (Figure 1c). After 1 h, the turbid solution diffused from the interface to the whole solution, indicating that more aggregates formed. These observation are further confirmed by optical microscopy (OM), polarized optical microscopy (POM), fluorescence optical microscopy (FOM), and transmission electron microscopy (TEM).

OM is used to characterize the morphology of these assemblies (Figure 1d). As shown in Figure S10, the average length and standard deviation were determined from the histogram of the microflowers to be 6.54 ± 1.85 μm. Anisotropic photoluminescence was observed when the flowers were placed between cross polarizers (inset), indicating the presence of ordered arrays of cage **1** within the microflowers. Autofluorescence of these microflowers was observed under UV irradiation (Figure 1e) and blue-light irradiation (Figure 1f) and attributed to the presence of the conjugated system in TPPE. No red emission was observed under green-light excitation (Figure S11). As shown in Figure 1g, these flower-like structures can also be observed by TEM, in good agreement with the SEM, OM, POM, and FOM results. In the TEM image in Figure 1h,i, the intersection between two needles was observed, indicating that the flower-like structures were formed through the stacking of needles and not by growth from one center. We detected some intermediates of the multilamellar structure that gradually converted to a needle during self-assembly, which suggests a possible mechanism of microneedle formation (by the stacking of thin layers). As shown in Figure 1j, the magnified needle has a width of 900 nm, suggesting that the microneedles are formed by the stacking of thin layers. Figure 1k shows an enlarged image of alternating lamellae, which demonstrates that the ordered arrangement of cage **1** plays a crucial role in the self-assembly. This observation is important since it highlights the significance of the stacked layer structure in the process of microneedle self-assembly. Since the dimensions of single cage **1** do not exceed 2.7 nm, the microneedles correspond to the alternating lamellae of cage **1**-based lamellae. The intermediate between the thin layers and microneedles was also observed. However, the mechanism of the formation of the microflowers remains unknown.

Many microneedles instead of microflowers were observed by OM (Figure 2a), suggesting that these microneedles might be the precursors of the microflowers. Autofluorescence was also observed under UV irradiation (Figure 2b) and blue-light irradiation (Figure 2c), in good agreement with the autofluorescence of the microflowers. Similar to Figure 1e,f, no red emission was observed under the green-light excitation. The intactness of cage **1** during assembly is essential to the resulting suprastructures. Therefore, the microneedles formed in 80% EA were centrifuged and redispersed in DCM, and then $^{31}P\{^1H\}$ and ^1H NMR spectra were obtained to determine the integrity of cage **1**. The $^{31}P\{^1H\}$ NMR spectrum of cage **1** in Figure S12 shows two doublets of approximately equal intensity at $\delta = 6.44$ and 0.62 ppm, with concomitant ^{195}Pt satellite peaks corresponding to two distinct phosphorus environments, demonstrating that the Pt(II) centers on cage **1** remain heteroligated. The ^1H NMR spectrum (Figure S13) also confirms that the metallacages were intact after assembly. As shown in Figure S14, the integrity of cage **1** was further supported by ESI-TOF-MS data, which showed an intact entity with charge states resulting from the loss of the OTf$^-$ counterions ($m/z = 2044.82$ for $[M - 3OTf]^{3+}$).

The arrangement of molecules in the assemblies was then characterized using small-angle X-ray scattering (SAXS) and powder X-ray diffraction (XRD) measurements (Figure 3a,b). Figure 3a shows a broad Bragg reflection peak centered at 0.058 Å^{-1}, corresponding to the ordered structure with an interlayer spacing of 10.8 nm. Given that the length (*x* axis), height (*y* axis), and width (*z* axis) for cage **1** (Figure 3c, Figure S15) are calculated as ca. 2.7 (*x* axis), 2.0 (*y* axis), and 2.4 nm (*z* axis), respectively, this SAXS observation demonstrates that the ordered structure with 10.8 nm interlayer spacing may have formed by the stacking of four cages (along the *x* axis direction). The assemblies then show a slight peak at a higher *q* value (0.121 Å^{-1}), corresponding to the ordered structure with an interlayer spacing of 5.2 nm (stacking of two cages along the *x* axis direction), which might be the second-order peak at ~0.058 Å^{-1}, characteristic of a crystalline lamellar packing system. However, these peaks are weak, possibly because of the partially inhomogeneous lamellar structure within the microneedles.

The first SAXS peak is centered on 0.058 Å^{-1} (10.8 nm), but this broad peak covers the *q* range from 0.031 to 0.082 Å^{-1}, corresponding to an interlayer spacing between 7.7 and 20.3 nm. The second SAXS peak is centered at 0.121 Å^{-1} (5.2 nm), but this broad peak covers a *q* range from 0.110 to 0.130 Å^{-1}, corresponding to an interlayer spacing between 4.8 and 5.7 nm. This broad range might be caused by the similar size among the length (2.7 nm), the height (2.0 nm), and the width (2.4 nm) for cage **1**, leading to the overlap of three peaks (2.7, 2.0, and 2.4 nm).

The local molecular arrangements for these assemblies at wide-angle regions were also determined using powder XRD measurements (Figure 3b). The *d*-spacing corresponding to the intermolecular stacking is observed at 0.49 nm, in agreement with the π–π stacking distance between benzene rings,[56] which is similar to literature reports (typical π–π stacking). On the basis of these SAXS and XRD measurements, it is observed that there are multiple orders of structure within the assemblies.

To elucidate the differences in these assemblies as a function of the DCM/EA ratio, the concentration of the cage was fixed at 10 μM, leaving the proportion of EA/DCM in the system as the only variable. We found that changing the EA percentage (from 90% to 10%) still produced microneedles/microflowers, but the size and uniformity of the needles varied. As shown in Figure 4, the microflowers formed in the presence of 10%, 40%, and 70% EA were selected for systematic study. In the 10% EA mixture, microflowers together with some ill-defined structures could be observed (Figure 4a). As can be seen in Figure 4b, needle-like nanostructures could be observed by TEM. The average length and standard deviation were determined from their histogram (Figure 4c) to be 2.78 ± 0.52 nm. The average width and standard deviation were determined from their histogram (Figure 4d) to be 200 ± 9.00 nm. When the EA content was increased to 40%, rigid flower aggregates became the predominant species (Figure 4e).

TEM results show these one-dimensional structures with wider width and longer length, but multilayer structures were also observed (Figure 4f). As shown in Figure 4g,h, the average length and standard deviation were determined from their histogram to be 3.93 ± 1.05 μm (Figure 4g). The width of these microneedles increased with increasing EA content in the binary solvent. As can be seen in Figure 4h, the average width and standard deviation were determined from their histogram to be 260 ± 14.00 nm.

When the EA content was increased to 70%, flower aggregates with wider widths were the predominant species (Figure 4i). TEM observation further confirmed the multilayer structures (Figure 4j). The corresponding length and standard deviation were determined from their histogram to be 4.86 ± 1.40 μm (Figure 4k), and the width and standard deviation were determined to be 510 ± 90.00 nm (Figure 4l). When the EA percentage reached 90%, the flower structures were not as uniform as those previously observed (with larger deviations). As shown in Figure S16, the average length and standard deviation were 5.66 ± 1.86 μm, and the width of these microneedles increased with increasing EA content in the binary solvent. XRD revealed that the microflowers had similar structures. Compared with the system with lower EA% content, more assemblies could be centrifuged to meet the requirements for XRD characterization, and EA contents from 60% to 90% were selected for further study. As shown in Figure S17, a set of distinct diffraction peaks were observed, further supporting the SEM results and confirming that similar structures could be obtained by different using EA contents. In particular, all the assemblies showed distinct diffraction peaks at approximately $d \approx 0.49$ nm, close to the result for typical π–π stacking.

Figure S18 presents the fluorescence spectra of cage **1** in solutions with different ratios of DCM/EA (EA from 60% to 90%) at a concentration of 10 μM. All assemblies show a peak at approximately 450 nm. This result corresponds well with the SEM and XRD results. As shown in Figure S19, similar absorption bands were observed for the assemblies formed at different EA contents (EA from 70% to 90%), in good agreement with the SEM, XRD, and fluorescence spectra results.

The intermolecular interactions among cages **1** were investigated by ^{1}H NMR (Figure S20a–d). As shown in Figure S20a,b, the signals of H_{4a} and H_{4b} shift from 8.046 and 7.903 ppm (100% DCM, 0% EA) to 8.040 and 7.886 ppm (10% EA), to 8.038 and 7.882 ppm (20%

EA), and then to 8.030 and 7.867 ppm (30% EA). Furthermore, upfield (H_{2c} and H_{2d}) and downfield (H_{2a} and H_{2b}) chemical shifts were observed, which might be caused by the dicarboxylate ligands' (pillar) twist in the cages **1**.

The $^{31}P\{^1H\}$ NMR signals (Scheme 1, Figure S20e,h) of cage **1** in the DCM/EA mixture downfield shift from 5.88 and 0.09 ppm (100% DCM, 0% EA), to 6.00 and 0.25 ppm (10% EA), to 6.04 and 0.30 ppm (20% EA), and then to 6.13 and 0.44 ppm (30% EA). Furthermore, the signals become broader with the increase of EA content from 0% to 30% EA, which further indicates the interactions between the P atoms, due to the increase of interactions between these cages. DOSY ^1H NMR was used to obtain the diffusion of cage **1** in various DCM/EA mixtures. The measured weight-average diffusion coefficients were 4.81×10^{-10} m^2 s^{-1} for cage **1** in the mixture with 10% EA content (Figure S20i). The observation of the same diffusion coefficients of TPPE (H_{2a}, H_{2b}, H_{2c}, and H_{2c}) and the pillar (H_{4a}, H_{4b}, and H_{4c}) confirmed the integrity of cage **1**. In contrast, the measured weight-average diffusion coefficient of cage **1** in pure DCM was 5.22×10^{-10} m^2 s^{-1} (Figure S20j), which is lower than that in DCM/EA mixtures. These results further support the formation of aggregates in DCM/EA mixtures.

Microstructure examination via SEM at mixing times of 120 and 240 min revealed a gradual evolution of shapes and sizes of the resultant microstructures. It is found that the length and width increased with prolonged time (Figure S21). Elemental mapping analysis and SEM (Figure S22) indicated homogeneous distributions of N, O, Pt, F, S, and P across the microspheres, providing evidence that the microflowers were composed of TPPE, *cis*-Pt(PEt$_3$)$_2$(OTf)$_2$, and the carboxylate ligand. Furthermore, temperature has no obvious effect on the morphology (Figure S23).

We thus propose a possible mechanism for the formation of the microflowers, as illustrated in Scheme 2: the individual cage **1** molecules dissolve in DCM and stack via *π–π* interactions to form elongated one-dimensional supramolecular assemblies by the addition of EA, leading to the formation of microneedles (steps 1–3). The EA percentage plays an important role in the length and width of the microneedles formed, as their length and width increased with increasing EA content. Subsequently, cage **1**-based microflowers formed during solvent evaporation in a silica wafer/cropper grid (step 4). Magnification of the microflowers provides the stacking mode of cage **1**, as shown in black arrows, growing along the *x, y, z* axes (Figure 3c), which then produces the lamellar packing suprastructures, in turn resulting in the formation of the cage **1**-based microneedles and microflowers.

To broaden the emission range, a lysine-modified perylene (Figure S24) with red emission was used for co-assembly with the microneedles. Figure 5a–c shows typical SEM images of the microneedle structures after co-assembly, which indicate that the microneedles have high monodispersity and that each single needle has a uniform width along its entire length. Larger microneedles with broader widths were obtained that are several micrometers long. Figure 5b,c shows individual needles with lengths of approximately 10.30 ± 2.26 *μ*m (Figure 5d) and widths of approximately 670 ± 130 nm (Figure S25).

OM micrographs further confirmed the microflower morphology (Figure S26a). Anisotropic photoluminescence was also observed by a polarization microscope (Figure S26b), providing evidence for the presence of ordered arrays of cage **1** within the microflowers. Figure S26c shows that the individual needles have lengths of approximately 10.11 ± 2.00 nm.

The packing information with respect to the assemblies is shown in Figure S27. There was also a broad Bragg reflection peak centered at 0.051 $Å^{-1}$, corresponding to an ordered structure with an interlayer spacing of 12.3 nm. Autofluorescence was observed under UV irradiation (Figure 5e) and blue-light irradiation (Figure 5f) and was attributed to the presence of the conjugated system in TPPE. The lysine-modified perylene-containing microneedles and microflowers gave a red emission under green irradiation (Figure 5g), providing additional evidence for the presence of lysine-modified perylene in the microneedles/microflowers. The average length and standard deviation were determined from the histogram to be 12.69 ± 2.75 μm (Figure 5h), consistent with the SEM and OM results and the proposed mechanism of formation shown in Scheme 1 (step 5–9). The $^{31}P\{^1H\}$ NMR spectrum of cage **1** in Figure S28 shows two doublets of approximately equal intensity at $\delta = 5.78$ and -0.02 ppm, with concomitant ^{195}Pt satellite peaks corresponding to two distinct phosphorus environments, demonstrating the integrity of cage **1** after the co-assembly of lysine-modified perylene. No chemical shifts of cage **1** and lysine-modified perylene before and after mixing were observed, indicating that the interaction between cage **1** and the lysine-modified perylene is not a host-guest interaction but a simple physical adsorption (Figure S29).

Self-assembled one-dimensional suprastructures[57] have proven useful in the fabrication of functional materials.[58] Several groups have fabricated functional materials by utilizing 1D materials as templates[59] and investigated their application in bionanotechnology.[60] Inspired by the preparation of perylene/microneedles composites, we selected chlorophyll-a (Chl-a) as a model of a fat-soluble biomolecule for its potential application in the energy field (Chl-a serves as the light-absorbing and energy-transferring components in the assemblies). We selected vitamin B_{12} as a model of a water-soluble biomolecule for its potential application in biomedical sciences;[61] for example, it could modulate the transcriptome of the skin microbiota in acne pathogenesis.[62] Herein, we demonstrate the preparation of Chl-a- and vitamin B_{12}-containing microflowers by using cage **1**-based microneedles as a platform. By using the microneedles as a template, Chl-a and vitamin B_{12} are introduced by a "phase-transfer" strategy at room temperature.

It is well known that chloroplasts contain chlorophyll within their thylakoids, which absorbs light energy and gives chloroplasts their green color. Thus, in order to get chlorophyll-based functional material, Chl-a was used for the co-assembly with metallacage-based suprastructures. Figure 6a (right) shows that the initial brown solution (top layer)/white suspension (bottom layer) are converted into a homogeneous brown suspension, which suggests the formation of Chl-a/microneedle composites. Figure 6b,c shows the SEM images of the microneedle structures after co-assembly, indicating that microneedles were obtained. Furthermore, the $^{31}P\{^1H\}$ NMR spectrum (Figure 6d) of cage **1** shows two doublets of approximately equal intensity at $\delta = 6.16$ and 0.33 ppm, demonstrating the

integrity of cage **1** after the co-assembly with Chl-a. FOM was used to observe Chl-a-containing microneedles. As shown in Figure S30, the Chl-a-containing microneedles and microflowers gave a red emission under green-light excitation, providing evidence for the presence of Chl-a (from porphyrin) in the microneedles/microflowers. No chemical shifts of cage **1** and Chl-a before and after mixing were observed, indicating that the interaction between cage **1** and Chl-a is not a host–guest interaction but a simple physical adsorption (Figure S31).

Vitamin B_{12} was used to construct metallacage-based hybrid materials for its potential application in biomedical science, such as for nerve injury repair (Figure 6e, left). The initial pink solution (top layer)/white suspension (bottom layer) are converted into a homogeneous pink suspension (Figure 6e, inset), which suggests the formation of vitamin B_{12}/microneedle composites. Figure 6f,g shows the SEM images of the microneedle structures after co-assembly. The $^{31}P\{^{1}H\}$ NMR spectrum of cage **1** (Figure 6h) shows two doublets of approximately equal intensity at $\delta = 6.12$ and 0.26 ppm, demonstrating the integrity of cage **1** after the co-assembly with vitamin B12. Subsequently, FOM was used to observe microneedles (Figure S32). The vitamin B_{12}-containing microneedles and microflowers gave a red emission (from porphyrin), providing evidence for the presence of vitamin B_{12}. No chemical shifts of cage **1** and vitamin B_{12} before and after mixing were observed, indicating that the interaction between cage **1** and vitamin B_{12} is not a host–guest interaction but a simple physical adsorption (Figure S33).

CONCLUSION

The results described here demonstrate the capability of cage **1** to assemble into well-defined microneedles and microflowers. In contrast to previous studies that mainly dealt with the formation of metal–organic complexes with dimensions of nanometers, this work may open an alternative path for the preparation of metal–organic complexes in hierarchical assemblies. Furthermore, we successfully prepared metal–organic complex microneedle materials with controllable emission by using perylene as a co-assembly component. The introduction of various biomolecules into this supramolecular platform could provide diverse artificial biological units for mimicking and optimizing assembly-based synthetic systems. We anticipate that this methodology will open an avenue to a new and simple pathway to metal–organic complex-based hybrid materials and devices.

EXPERIMENTAL SECTION

Materials and Methods.

All reagents were commercially available and used as supplied without further purification. Deuterated solvents were purchased from Cambridge Isotope Laboratory (Andover, MA). Compounds **2, 8**, and **4**[46] were prepared according to modified literature procedures. NMR experiments were recorded at room temperature. ^{1}H NMR spectra were recorded in the designated solvents on a Varian Inova 400 MHz or a Bruker Avance 600 spectrometer. $^{31}P\{^{1}H\}$ NMR spectra were recorded on a Varian Unity 300 NMR spectrometer, and $^{31}P\{^{1}H\}$ NMR chemical shifts are referenced to an external unlocked sample of 85% H_3PO_4 (δ 0.0 ppm). Mass spectra were recorded on a Micromass Quattro II triple-quadrupole mass

spectrometer using electrospray ionization with a MassLynx operating system. Ultraviolet–visible experiments were conducted on a Hitachi U-4100 absorption spectrophotometer. Fluorescence experiments were conducted on a Hitachi F-7000 fluorescence spectrophotometer.

Synthesis of Cage 1.

Tetra(4-pyridylphenyl)ethylene (compound **5**, 3.20 mg, 5.00 μmol), *cis*-Pt(PEt$_3$)$_2$(OTf)$_2$ (**6**, 14.60 mg, 20.0 μmol), and carboxylate ligand **8** (2.20 mg, 10.0 μmol) were placed in a 2-dram vial, followed by the addition of H$_2$O (0.40 mL) and acetone (1.20 mL). After the mixture was heated at 70 °C for 24 h, all the solvent was removed by a N$_2$ flow, and the solid was dried under vacuum. Acetone (1.00 mL) was then added to the resultant mixture, and the solution was stirred for 30 min at room temperature. The mixture was filtered to remove insoluble materials. The resulting tetragonal cage **1** was precipitated with diethyl ether, isolated, dried under reduced pressure, and dissolved in CD$_2$Cl$_2$ for characterization. The ^{31}P{^{1}H} NMR spectrum of tetragonal cage **1** is shown in Figure S1. ^{31}P{^{1}H} NMR (CD$_2$Cl$_2$, room temperature, 121.4 MHz) δ (ppm): 6.19, 0.38. The ^{1}H NMR spectrum of tetragonal cage **1** is shown in Figure S2. ^{1}H NMR (CD$_2$Cl$_2$, room temperature, 400 MHz) δ (ppm): 8.66 (d, 16H), 8.04 (s, 4H), 7.89 (d, 8H), 7.71 (d, 16H), 7.49 (d, 16H), 7.18 (d, 16H). The stoichiometry of discrete cages is further supported by the ESI-TOF-MS results. ESI-TOF-MS (m/z): calcd for [M − 3OTf]$^{3+}$ (C$_{225}$H$_{317}$F$_{15}$N$_8$O$_{31}$P$_{16}$Pt$_8$S$_5^{3+}$), 2044.84 (100%); found, 2044.83. Fragment, calcd for [M/2 − 2OTC]$^{2+}$ (C$_{112}$H$_{160}$F$_6$N$_4$O$_{14}$P$_8$Pt$_4$S$_2^{2+}$), 1495.89 (100%); found, 1495.90.

Self-Assembly of Cage 1 in DCM/EA.

In a typical experiment to prepare microneedles, 100 μL of DCM solution of cage **1** (100 μM) and 100 μL of DCM were mixed in a vial, and then 800 μL of EA was slowly added over 1 h. For other assemblies, a similar procedure using different amounts of DCM/EA solutions was applied to tune the ratio of DCM/EA in order to obtain assemblies with controllable length and width.

Co-Assembly of Cage 1-Based Microneedles with Lysine-Modified Perylene.

For preparation via co-assembly, cage **1**-based microneedles (10 μM) in DCM/EA with perylene (1 mM) were dissolved in THF to yield a DCM/EA/THF solution. In a typical experiment, 200 μL of DCM solution of cage **1** (100 μM) and 200 μL of DCM were mixed in a vial. Next, 1600 μL of EA was slowly added over 1 h, followed by the addition of 500 μL of 100 μM perylene to induce the co-assembly of cage **1**-based microneedles with perylene.

Co-Assembly of Cage 1-Based Microneedles with Chlorophyll-a.

For preparation via co-assembly, cage **1**-based microneedles (10 μM) in DCM/EA with Chl-a (1 mM) were dissolved in THF to yield a DCM/EA/THF solution. In a typical experiment, 200 μL of DCM solution of cage **1** (100 μM) and 200 μL of DCM were mixed in a vial. Next, 1600 μL of EA was slowly added over 1 h, followed by the addition of 200 μL of THF

and 500 μL of a 100 μM Chl-a ethanol solution to induce the co-assembly of cage **1**-based microneedles with Chl-a.

Co-Assembly of Cage 1-Based Microneedles with Vitamin B$_{12}$.

For preparation via co-assembly, cage **1**-based microneedles (10 μM) in DCM/EA with vitamin B$_{12}$ (1 mM) were dissolved in THF to yield a DCM/EA/THF solution. In a typical experiment, 200 μL of DCM solution of cage **1** (100 μM) and 200 μL of DCM were mixed in a vial. Next, 1600 μL of EA was slowly added over 1 h, followed by the addition of 200 μL of THF and 500 μL of a 100 μM vitamin B$_{12}$ ethanol solution to induce the co-assembly of cage **1**-based microneedles with vitamin B$_{12}$.

NMR Experiments.

^{1}H NMR and ^{31}P{^{1}H} NMR were used to get insight into the interactions between cage **1** and DCM/EA and the stability of cage**1** in DCM/EA. NMR spectra were recorded on a spectrometer at room temperature. The signal of the assemblies (final concentration: 100 μM) could not be detected due to their insolubility at EA contents greater than 30%. Thus, the signal could only be measured when the EA% was 0–30%, and these samples were measured to provide information about the interactions among assemblies. In a typical experiment to prepare a NMR sample, 100 μL of a CD$_2$Cl$_2$ solution of cage **1** (1 mM) and 900 μL of CD$_2$Cl$_2$ were mixed in a vial to get the solution of cage **1** with 0% EA. Separately, 100 μL of a CD$_2$Cl$_2$ solution of cage **1** (1 mM) and 800 μL of CD$_2$Cl$_2$ were mixed in a vial, and then 100 μL of EA was slowly added to get the solution of cage **1** with 10% EA; 100 μL of CD$_2$Cl$_2$ solution of cage **1** (1 mM) and 700 μL of CD$_2$Cl$_2$ were mixed in a vial, and then 200 μL of EA was slowly added to get the solution of cage **1** with 20% EA; and 100 μL of CD$_2$Cl$_2$ solution of cage **1** (1 mM) and 600 μL of CD$_2$Cl$_2$ were mixed in a vial, and then 300 μL of EA was slowly added to get the solution of cage **1** with 30% EA. For solutions of cage 1 with EA content beyond 30%, sediment appears rapidly, which is not suitable for NMR characterization.

OM Experiments.

OM and POM images were obtained using a Leica Microsystems DM LM/P instrument. FOM images were acquired on an Olympus IX73 W.D. 27 mm inverted microscope. For OM, POM, and FOM, dispersions of aggregates were dried onto glass slides for observation.

TEM Experiments.

TEM investigations were performed on a JEM-2100EX instrument. For TEM, dispersions of the assemblies were dried onto carbon-coated copper support grids. HRTEM images were obtained using a Tecnai G2 F30 S-TWIN instrument.

SEM Experiments.

A Zeiss Supra55 field-emission scanning electron microscope was used to investigate the assemblies. For SEM, dispersions of the assemblies were dried onto silicon wafers.

SAXS Experiments.

SAXS experiments were performed at room temperature on a NanoSTAR system (Bruker-AXS, 30 W). For SAXS, dispersions were loaded into special quartz X-ray capillary tubes with an internal diameter of 1.5 mm. In a typical experiment to prepare a SAXS sample, 100 μL of a DCM solution of cage **1** (100 μM) and 100 μL of DCM were mixed in a vial, and then 800 μL of EA was slowly added to get the solution of cage **1** with 80% EA.

XRD Experiments.

XRD data were taken with Cu Kα radiation ($\lambda = 0.154$ nm) on a D8 Advance powder diffractometer (Bruker), operated in the 10–40° (2θ) range and at a step scan of 2$\theta = 0.02$°. The tube voltage was 40 kV, and the tube current was 40 mA. The samples were prepared as a thin film on a glass plate through evaporation of the solvents. In a typical experiment to prepare an XRD sample, 100 μL of a DCM solution of cage **1** (100 μM) was used, and then 900 μL of EA was slowly added to get the solution of cage **1** with 90% EA. Separately, 100 μL of a DCM solution of cage **1** (1 mM) and 100 μL of DCM were mixed in a vial, and then 800 μL of EA was slowly added into above solution to get the solution of cage **1** with 80% EA; 100 μL of a DCM solution of cage **1** (1 mM) and 200 μL of DCM were mixed in a vial, and then 700 μL of EA was slowly added to get the solution of cage **1** with 70% EA. For solutions of cage **1** with EA content below 70%, evaporation on a glass plate to form a thin film could not cover the transparent glass substrate efficiently, which is not suitable for XRD characterization.

Supplementary Material

Refer to Web version on PubMed Central for supplementary material.

ACKNOWLEDGMENTS

REFERENCES

(1). Nagle JF; Tristram-Nagle S Structure of lipid bilayers. Biochim. Biophys. Acta, Rev. Biomembr 2000, 1469, 159.

(2). Dobson CM Protein folding and misfolding. Nature 2003, 426, 884. [PubMed: 14685248]

(3). Whitesides GM; Grzybowski B Self-assembly at all scales. Science 2002, 295, 2418. [PubMed: 11923529]

(4). Vale RD The molecular motor toolbox for intracellular transport. Cell 2003, 112, 467. [PubMed: 12600311]

(5). Poulos TL Heme enzyme structure and function. Chem. Rev 2014, 114, 3919. [PubMed: 24400737]

(6). Ke Z; Strauss JD; Hampton CM; Brindley MA; Dillard RS; Leon F; Lamb KM; Plemper RK; Wright ER Promotion of virus assembly and organization by the measles virus matrix protein. Nat. Commun 2018, 9, 1736. [PubMed: 29712906]

(7). Clarke NI; Royle SJ FerriTag is a new genetically-encoded inducible tag for correlative light-electron microscopy. Nat. Commun 2018, 9, 2604. [PubMed: 29973588]

(8). Grzybowski BA; Fitzner K; Paczesny J; Granick S From dynamic self-assembly to networked chemical systems. Chem. Soc. Rev 2017, 46, 5647. [PubMed: 28703815]

(9). Mozhdehi D; Luginbuhl KM; Simon JR; Dzuricky M; Berger R; Varol HS; Huang FC; Buehne KL; Mayne NR; Weitzhandler I; Bonn M; Parekh SH; Chilkoti A Genetically encoded lipid-polypeptide hybrid biomaterials that exhibit temperature-triggered hierarchical self-assembly. Nat. Chem 2018, 10, 496. [PubMed: 29556049]

(10). Matosevic S; Paegel BM Layer-by-layer cell membrane assembly. Nat. Chem 2013, 5, 958. [PubMed: 24153375]

(11). Siavashpouri M; Wachauf CH; Zakhary MJ; Praetorius F; Dietz H; Dogic Z Molecular engineering of chiral colloidal liquid crystals using DNA origami. Nat. Mater 2017, 16, 849. [PubMed: 28530665]

(12). Mohammadi E; Zhao C; Meng Y; Qu G; Zhang F; Zhao X; Mei J; Zuo J-M; Shukla D; Diao Y Dynamic-template-directed multiscale assembly for large-area coating of highly-aligned conjugated polymer thin films. Nat. Commun 2017, 8, 16070. [PubMed: 28703136]

(13). Avakyan N; Greschner AA; Aldaye F; Serpell CJ; Toader V; Petitjean A; Sleiman HF Reprogramming the assembly of unmodified DNA with a small molecule. Nat. Chem 2016, 8, 368. [PubMed: 27001733]

(14). Wagenbauer KF; Sigl C; Dietz H Gigadalton-scale shape-programmable DNA assemblies. Nature 2017, 552, 78. [PubMed: 29219966]

(15). Xiao Y; Sun H; Du J Sugar-Breathing Glycopolymersomes for Regulating Glucose Level. J. Am. Chem. Soc 2017, 139, 7640. [PubMed: 28508651]

(16). Sun Y; Guo F; Zuo T; Hua J; Diao G Stimulus-responsive light-harvesting complexes based on the pillararene-induced co-assembly of β-carotene and chlorophyll. Nat. Commun 2016, 7, 12042. [PubMed: 27345928]

(17). Avakyan N; Greschner AA; Aldaye F; Serpell CJ; Toader V; Petitjean A; Sleiman HF Reprogramming the assembly of unmodified DNA with a small molecule. Nat. Chem 2016, 8, 368. [PubMed: 27001733]

(18). Singh G; Chan H; Baskin A; Gelman E; Repnin N; Kral P; Klajn R Self-assembly of magnetite nanocubes into helical superstructures. Science 2014, 345, 1149. [PubMed: 25061133]

(19). Ong LL; Hanikel N; Yaghi OK; Grun C; Strauss MT; Bron P; Lai-Kee-Him J; Schueder F; Wang B; Wang P; Kishi JY; Myhrvold C; Zhu A; Jungmann R; Bellot G; Ke Y; Yin P Programmable self-assembly of three-dimensional nanostructures from 10,000 unique components. Nature 2017, 552, 72. [PubMed: 29219968]

(20). Guo J; Tardy BL; Christofferson AJ; Dai Y; Richardson JJ; Zhu W; Hu M; Ju Y; Cui J; Dagastine RR; Yarovsky I; Caruso F Modular assembly of superstructures from polyphenol-functionalized building blocks. Nat. Nanotechnol 2016, 11, 1105. [PubMed: 27723730]

(21). Saha ML; Yan X; Stang PJ Photophysical Properties of Organoplatinum(II) Compounds and Derived Self-Assembled Metallacycles and Metallacages: Fluorescence and its Applications. Acc. Chem. Res 2016, 49, 2527. [PubMed: 27736060]

(22). McConnell AJ; Wood CS; Neelakandan PP; Nitschke JR Stimuli-Responsive Metal-Ligand Assemblies. Chem. Rev 2015, 115, 7729. [PubMed: 25880789]

(23). Blanco V; Leigh DA; Marcos V Artificial switchable catalysts. Chem. Soc. Rev 2015, 44, 5341. [PubMed: 25962337]

(24). Han M; Michel R; He B; Chen Y-S; Stalke D; John M; Clever GH Angew. Chem. Light-triggered guest uptake and release by a photochromic coordination cage. Angew. Chem., Int. Ed 2013, 52, 1319.

(25). Wei P; Yan X; Huang F Supramolecular polymers constructed by orthogonal self-assembly based on host-guest and metal-ligand interactions. Chem. Soc. Rev 2015, 44, 815. [PubMed: 25423355]

(26). Durola F; Heitz V; Reviriego F; Roche C; Sauvage J-P; Sour A; Trolez Y Cyclic [4] rotaxanes containing two parallel porphyrinic plates: toward switchable molecular receptors and compressors. Acc. Chem. Res 2014, 47, 633. [PubMed: 24428574]

(27). Zarra S; Wood DM; Roberts DA; Nitschke JR Molecular containers in complex chemical systems. Chem. Soc. Rev 2015, 44, 419. [PubMed: 25029235]

(28). Zhang D; Ronson TK; Mosquera J; Martinez A; Nitschke JR Selective Anion Extraction and Recovery Using a FeII 4 L4 Cage. Angew. Chem., Int. Ed 2018, 57, 3717.

(29). Pilgrim BS; Roberts DA; Lohr TG; Ronson TK; Nitschke JR Signal transduction in a covalent post-assembly modification cascade. Nat. Chem 2017, 9, 1276.

(30). Roberts DA; Pilgrim BS; Sirvinskaite G; Ronson TK; Nitschke JR Covalent Post-assembly Modification Triggers Multiple Structural Transformations of a Tetrazine-Edged Fe4L6 Tetrahedron. J. Am. Chem. Soc 2018, 140, 9616. [PubMed: 29983061]

(31). Kassem S; Lee STL; Leigh DA; Marcos V; Palmer LI; Pisano S Stereodivergent synthesis with a programmable molecular machine. Nature 2017, 549, 374. [PubMed: 28933436]

(32). De Bo G; Gall MAY; Kuschel S; De Winter J; Gerbaux P; Leigh DA An artificial molecular machine that builds an asymmetric catalyst. Nat. Nanotechnol 2018, 13, 381. [PubMed: 29610529]

(33). Cremers J; Haver R; Rickhaus M; Gong JQ; Favereau L; Peeks MD; Claridge TDW; Herz LM; Anderson HL Template-Directed Synthesis of a Conjugated Zinc Porphyrin Nanoball. J. Am. Chem. Soc 2018, 140, 5352. [PubMed: 29638125]

(34). Ueda Y; Ito H; Fujita D; Fujita M Permeable Self-Assembled Molecular Containers for Catalyst Isolation Enabling Two-Step Cascade Reactions. J. Am. Chem. Soc 2017, 139, 6090. [PubMed: 28402111]

(35). Uchida J; Yoshio M; Sato S; Yokoyama H; Fujita M;Kato T Self-Assembly of Giant Spherical Liquid-Crystalline Complexes and Formation of Nanostructured Dynamic Gels Exhibiting Self-Healing Properties. Angew. Chem 2017, 129, 14273.

(36). Cao L; Wang P; Miao X; Dong Y; Wang H; Duan H; Yu Y; Li X; Stang PJ Diamondoid Supramolecular Coordination Frameworks from Discrete Adamantanoid Platinum(II) Cages. J. Am. Chem. Soc 2018, 140, 7005. [PubMed: 29746782]

(37). Tian Y; Yan X; Saha ML; Niu Z; Stang PJ Hierarchical Self-Assembly of Responsive Organoplatinum(II) Metallacycle-TMV Complexes with Turn-On Fluorescence. J. Am. Chem. Soc 2016, 138, 12033. [PubMed: 27608138]

(38). Kuritani M; Tashiro S; Shionoya M Organic and Organometallic Nanofibers Formed by Supramolecular Assembly of Diamond-Shaped Macrocyclic Ligands and PdII Complexes. Chem. - Asian J 2013, 8, 1368. [PubMed: 23554351]

(39). Xu XD; Yao CJ; Chen LJ; Yin GQ; Zhong YW; Yang HB Facile Construction of Structurally Defined Porous Membranes from Supramolecular Hexakistriphenylamine Metallacycles through Electropolymerization. Chem. - Eur. J 2016, 22, 5211. [PubMed: 26771048]

(40). Yin GQ; Chen L; Wang CH; Yang HB Fabrication of Neutral Supramolecular Polymeric Films via Post-electropolymerization of Discrete Metallacycles. Chin. J. Chem 2018, 36, 134.

(41). Zheng W; Yang G; Shao N; Chen LJ; Ou B; Jiang ST; Chen G; Yang HB CO2 Stimuli-Responsive, Injectable Block Copolymer Hydrogels Cross-Linked by Discrete Organoplatinum(II) Metallacycles via Stepwise Post-Assembly Polymerization. J. Am. Chem. Soc 2017, 139, 13811. [PubMed: 28885839]

(42). Sun Y; Li S; Zhou Z; Saha ML; Datta S; Zhang M; Yan X; Tian D; Wang H; Wang L; Li X; Liu M; Li H; Stang PJ Alanine-Based Chiral Metallogels via Supramolecular Coordination Complex Platforms: Metallogelation Induced Chirality Transfer. J. Am. Chem. Soc 2018, 140, 3257. [PubMed: 29290113]

(43). Zhukhovitskiy AV; Zhong M; Keeler EG; Michaelis VK; Sun JE; Hore MJ; Pochan DJ; Griffin RG; Willard AP; Johnson JA Highly branched and loop-rich gels via formation of metal-or-ganic cages linked by polymers. Nat. Chem 2016, 8, 33. [PubMed: 26673262]

(44). Foster JA; Parker RM; Belenguer AM; Kishi N; Sutton S; Abell C; Nitschke JR Differentially Addressable Cavities within Metal-Organic Cage-Cross-Linked Polymeric Hydrogels. J. Am. Chem. Soc 2015, 137, 9722. [PubMed: 26153733]

(45). Piot M; Abecassis B; Brouri D; Troufflard C; Proust A; Izzet G Control of the hierarchical self-assembly of polyoxometalate based metallomacrocycles by redox trigger and solvent composition. Proc. Natl. Acad. Sci. U. S. A 2018, 115, 8895. [PubMed: 30131428]

(46). Yan X; Cook TR; Wang P; Huang F; Stang p. J. Highly emissive platinum(II) metallacages. Nat. Chem 2015, 7, 342. [PubMed: 25803473]

(47). Zhang M; Li S; Yan X; Zhou Z; Saha ML; Wang YC; Stang PJ Fluorescent metallacycle-cored polymers via covalent linkage and their use as contrast agents for cell imaging. Proc. Natl. Acad. Sci. U. S. A 2016, 113, 11100. [PubMed: 27647900]

(48). Chen LJ; Ren YY; Wu NW; Sun B; Ma JQ; Zhang L; Tan H; Liu M; Li X; Yang HB Hierarchical Self-Assembly of Discrete Organoplatinum (II) Metallacycles with Polysaccharide via Electrostatic Interactions and Their Application for Heparin Detection. J. Am. Chem. Soc 2015, 137, 11725. [PubMed: 26322626]

(49). Yu G; Zhang M; Saha ML; Mao Z; Chen J; Yao Y; Zhou Z; Liu Y; Gao C; Huang F; Chen X; Stang PJ Antitumor Activity of a Unique Polymer That Incorporates a Fluorescent Self-Assembled Metallacycle. J. Am. Chem. Soc 2017, 139, 15940. [PubMed: 29019660]

(50). Yan X; Xu JF; Cook TR; Huang F; Yang QZ; Tung CH; Stang PJ Photoinduced transformations of stiff-stilbene-based discrete metallacycles to metallosupramolecular polymers. Proc. Natl. Acad. Sci. U. S. A 2014, 111, 8717. [PubMed: 24889610]

(51). Zhou Z; Yan X; Cook TR; Saha ML; Stang PJ Engineering Functionalization in a Supramolecular Polymer: Hierarchical Self-Organization of Triply Orthogonal Non-covalent Interactions on a Supramolecular Coordination Complex Platform. J. Am. Chem. Soc 2016, 138, 806. [PubMed: 26761393]

(52). Lu C; Zhang M; Tang D; Yan X; Zhang Z; Zhou Z; Song B; Wang H; Li X; Yin S; Sepehrpour H; Stang PJ Fluorescent Metallacage-Core Supramolecular Polymer Gel Formed by Orthogonal Metal Coordination and Host-Guest Interactions. J. Am. Chem. Soc 2018, 140, 7674. [PubMed: 29856215]

(53). Shankar S; Balgley R; Lahav M; Cohen SR; Popovitz-Biro R; van der Boom ME Metal-Organic Microstructures: From Rectangular to Stellated and Interpenetrating Polyhedra. J. Am. Chem. Soc 2015, 137 (1), 226. [PubMed: 25469935]

(54). di Gregorio M; Ranjan P; Houben L; Shimon LJW; Rechav K; Lahav M; van der Boom ME Metal-Coordination-Induced Fusion Creates Hollow Crystalline Molecular Superstructures. J. Am. Chem. Soc 2018, 140 (29), 9132. [PubMed: 29939733]

(55). Sun Y; Yao Y; Wang H; Fu W; Chen C; Saha ML; Zhang M; Datta S; Zhou Z; Yu H; Li X; Stang PJ Self-Assembly of Metallacages into Multidimensional Suprastructures with Tunable Emissions. J. Am. Chem. Soc 2018, 140 (40), 12819. [PubMed: 30212221]

(56). Sun Y; Li Z-B; Wang Z-HJ Mater. Chem 2012, 22, 4312.

(57). Nagaoka Y; Tan R; Li R; Zhu H; Eggert D; Wu YA; Liu Y; Wang Z; Chen O Superstructures generated from truncated tetrahedral quantum dots. Nature 2018, 561, 378. [PubMed: 30232427]

(58). Cheng H; Hu C; Zhao Y; Qu L Graphene fiber: a new material platform for unique applications. NPG Asia Mater 2014, 6, No. e113.

(59). Sun Y; Yao Y; Yan CG; Han Y; Shen M Selective decoration of metal nanoparticles inside or outside of organic microstructures via self-assembly of resorcinarene. ACS Nano 2010, 4, 2129. [PubMed: 20235516]

(60). Amit M; Yuran S; Gazit E; Reches M; Ashkenasy N Tailor-Made Functional Peptide Self-Assembling Nanostructures. Adv. Mater 2018, 30, 1707083.

(61). Elbaz B; Traka M; Kunjamma RB; Dukala D; Brosius Lutz A; Anton ES; Barres BA; Soliven B; Popko BAdenomatous polyposis coli regulates radial axonal soring and myelination in the PNS. Development 2016, 143, 2356. [PubMed: 27226321]

(62). Kang D; Shi B; Erfe MC; Craft N; Li H Vitamin B12 modulates the transcriptome of the skin microbiota in acne pathogenesis. Sci. Transl. Med 2015, 7, 293–103.
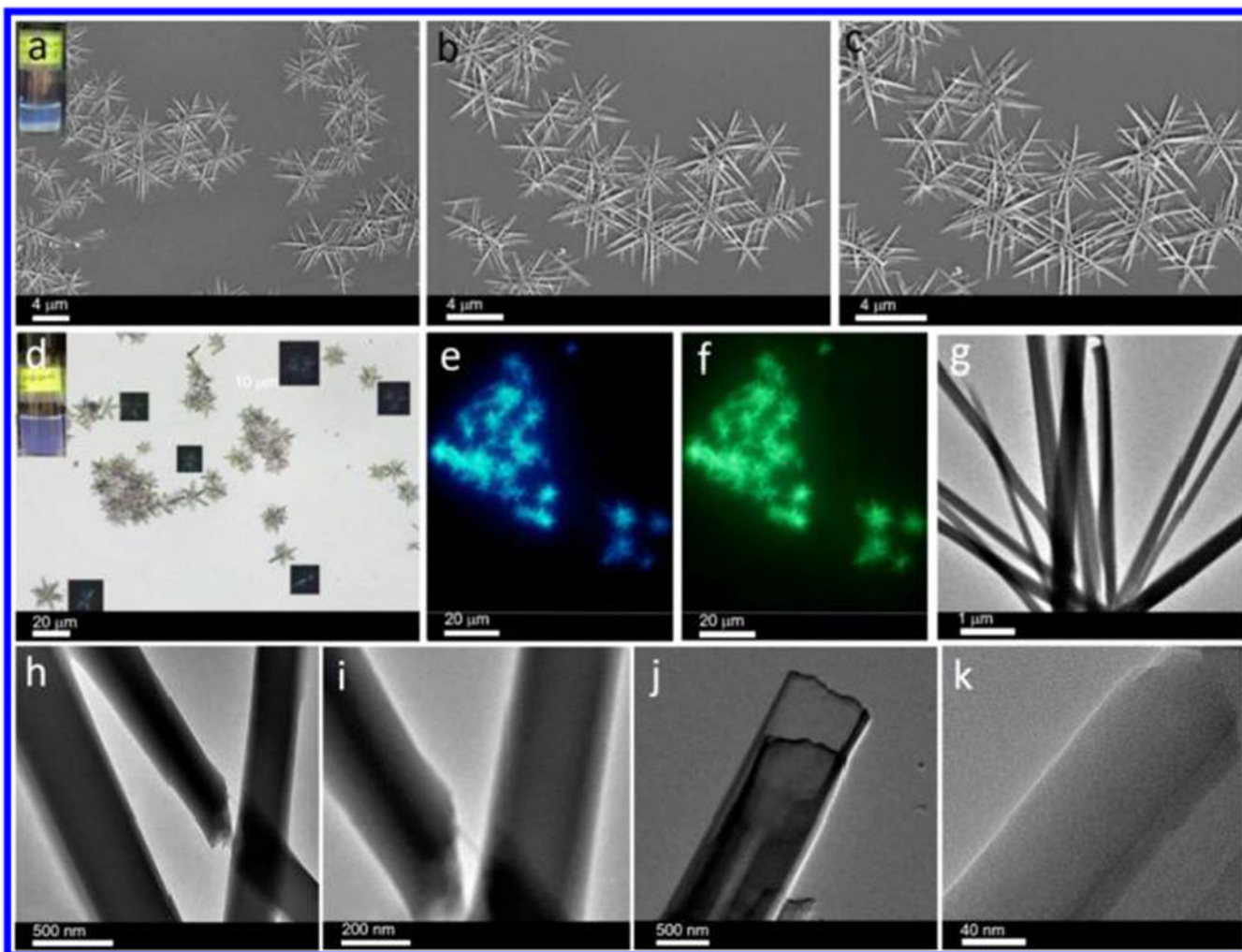
Figure 1.
(a) SEM images of microneedle-based microflowers formed by cage **1** (10 μM) in a DCM/EA mixture with 80% EA (inset: optical image showing the assembly method in binary solvents). (b,c) Corresponding assemblies at different magnifications. (d) Optical microscopy image of cage **1**-based assemblies (10 μM) over a large area (inset: corresponding digital photo and polarized optical microscopy image). (e,f) Fluorescence microscopy images of these assemblies under (e) ultraviolet-light excitation and (f) blue-light excitation. (g) TEM image of microflowers formed by cage **1** (10 μM). (h) TEM image showing the intersection between two needles. (i,j) TEM images showing the multilayer structures. (k) Magnified TEM image of the layer structure.
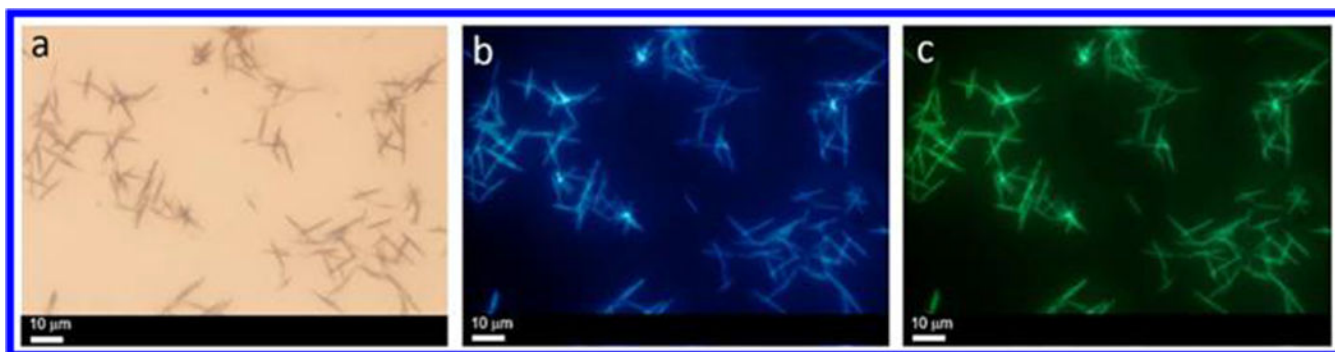
Figure 2.
(a) Optical microscopy image of cage 1-based assemblies (10 μM). Fluorescence microscopy images of these assemblies under ultraviolet-light excitation and (c) blue-light excitation.
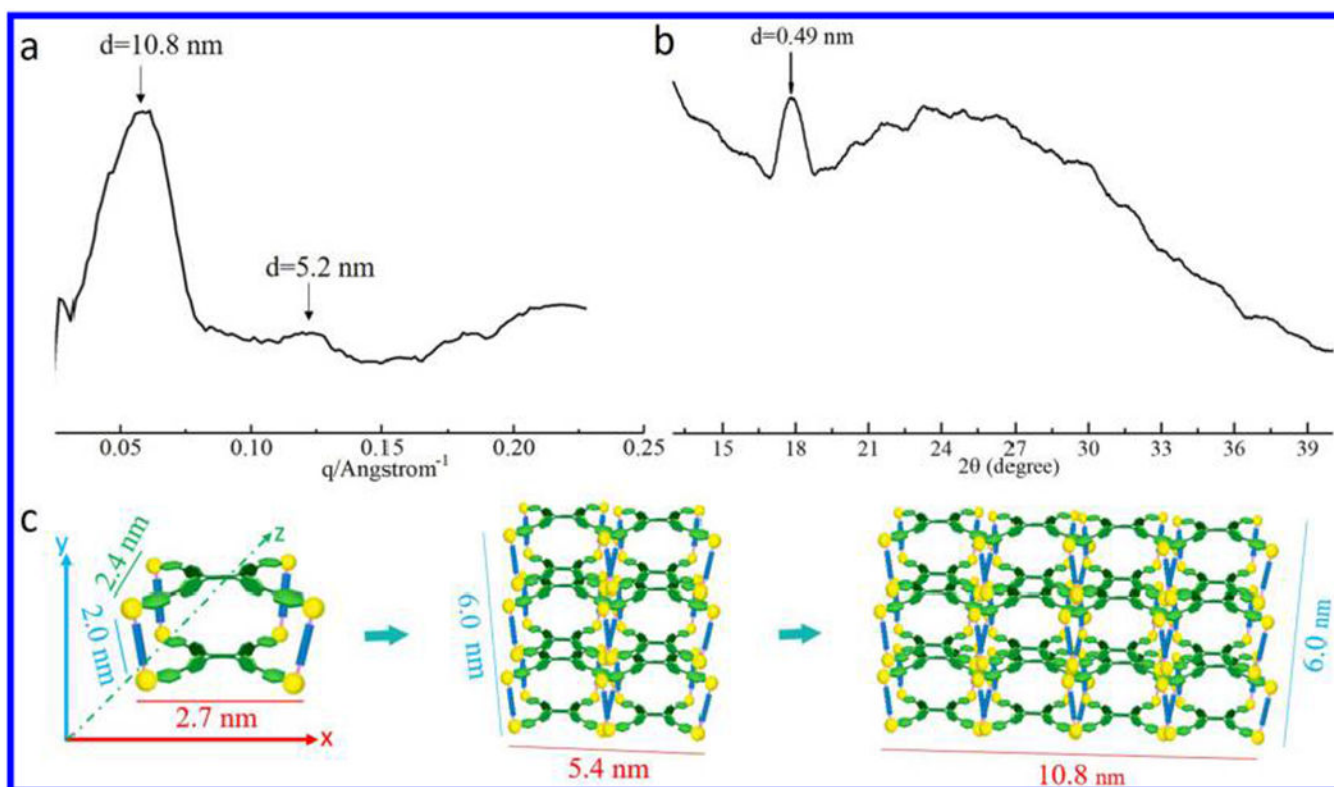
Figure 3.
(a) SAXS profile of cage **1** in DCM/EA mixture with 80% EA. (b) Corresponding XRD
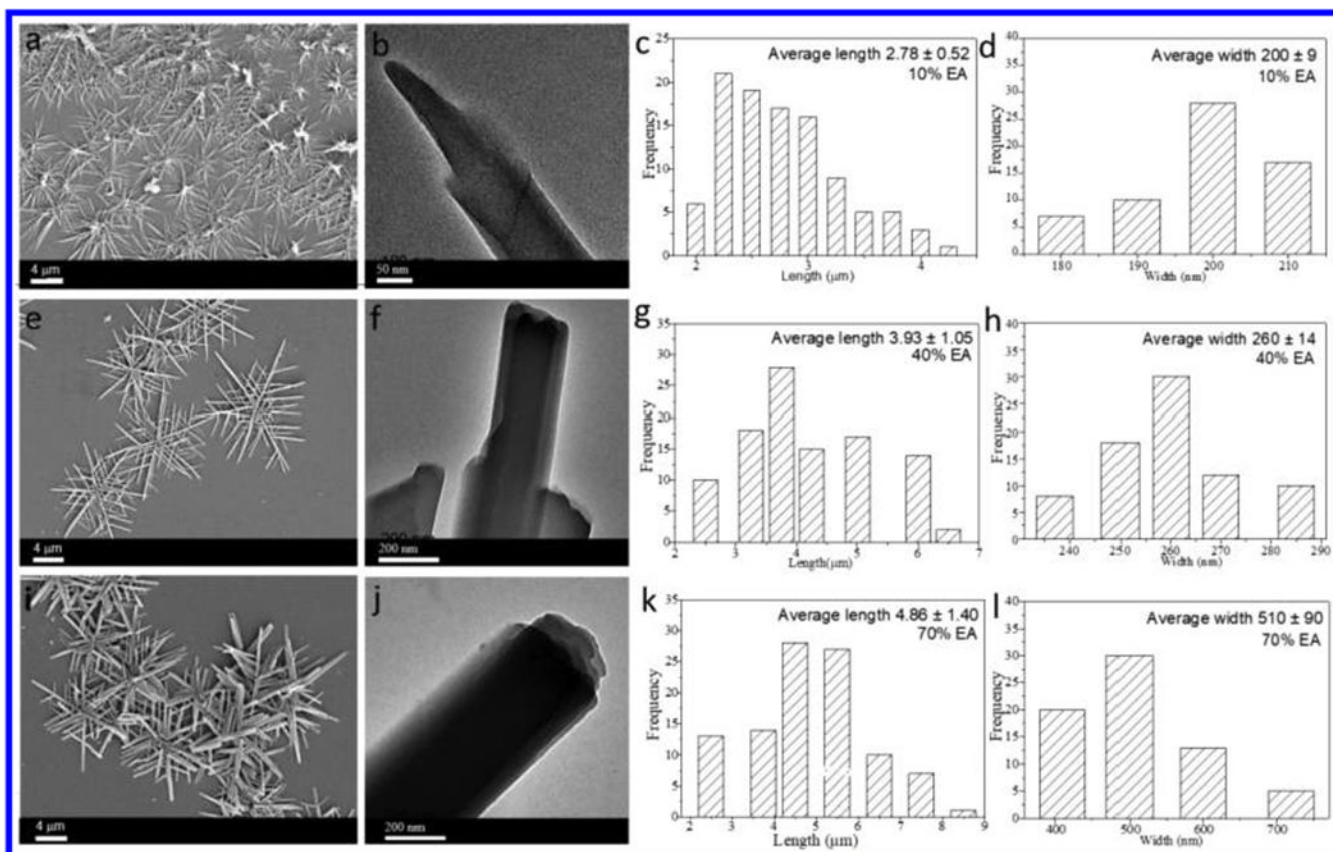profile. (c) Proposed stacking mode of cage **1**.

Figure 4.
SEM images and corresponding size histogram of nanostructures formed from cage **1** (10 μM) in DCM/EA mixtures (freshly prepared) with 10% (a–d), 40% (e–h), and 70% EA (i–l).

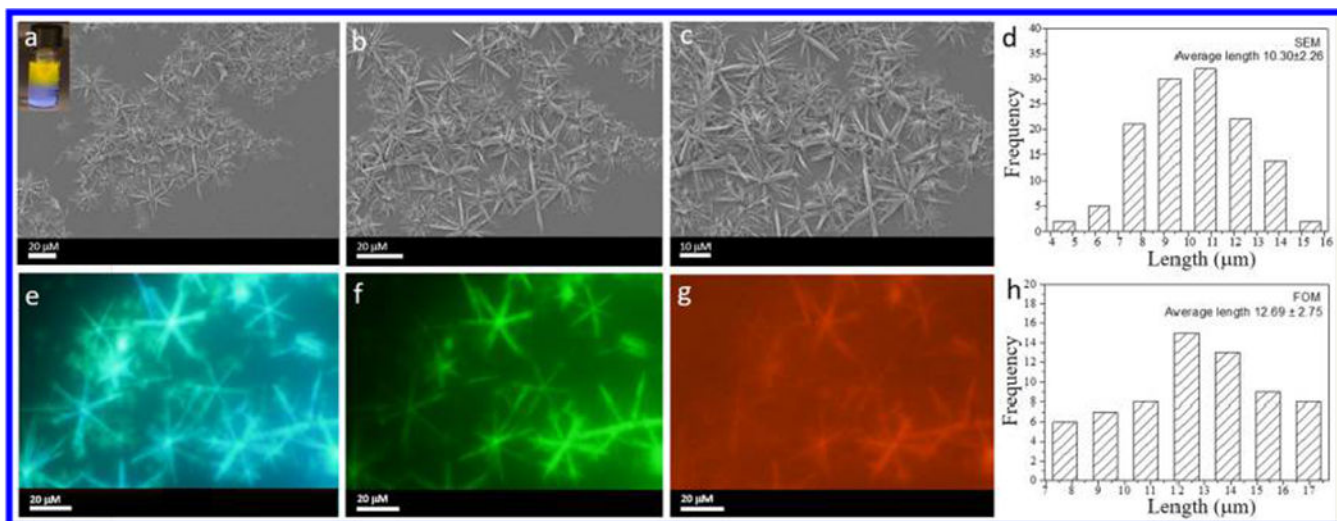**Figure 5.**
(a) SEM images of needle-based flowers formed by cage **1** (10 μM) in a DCM/EA mixture with 80% EA and lysine-modified perylene (inset: optical image showing the "phase-transfer" co-assembly process). (b,c) SEM images of the corresponding assemblies at different magnifications. (d) Histogram of the size distribution of the assemblies according to SEM. Fluorescence microscopy images of the assemblies under (e) ultraviolet-light excitation, (f) blue-light excitation, and (g) green-light excitation. (h) Histogram of the size distribution of the assemblies according to FOM.
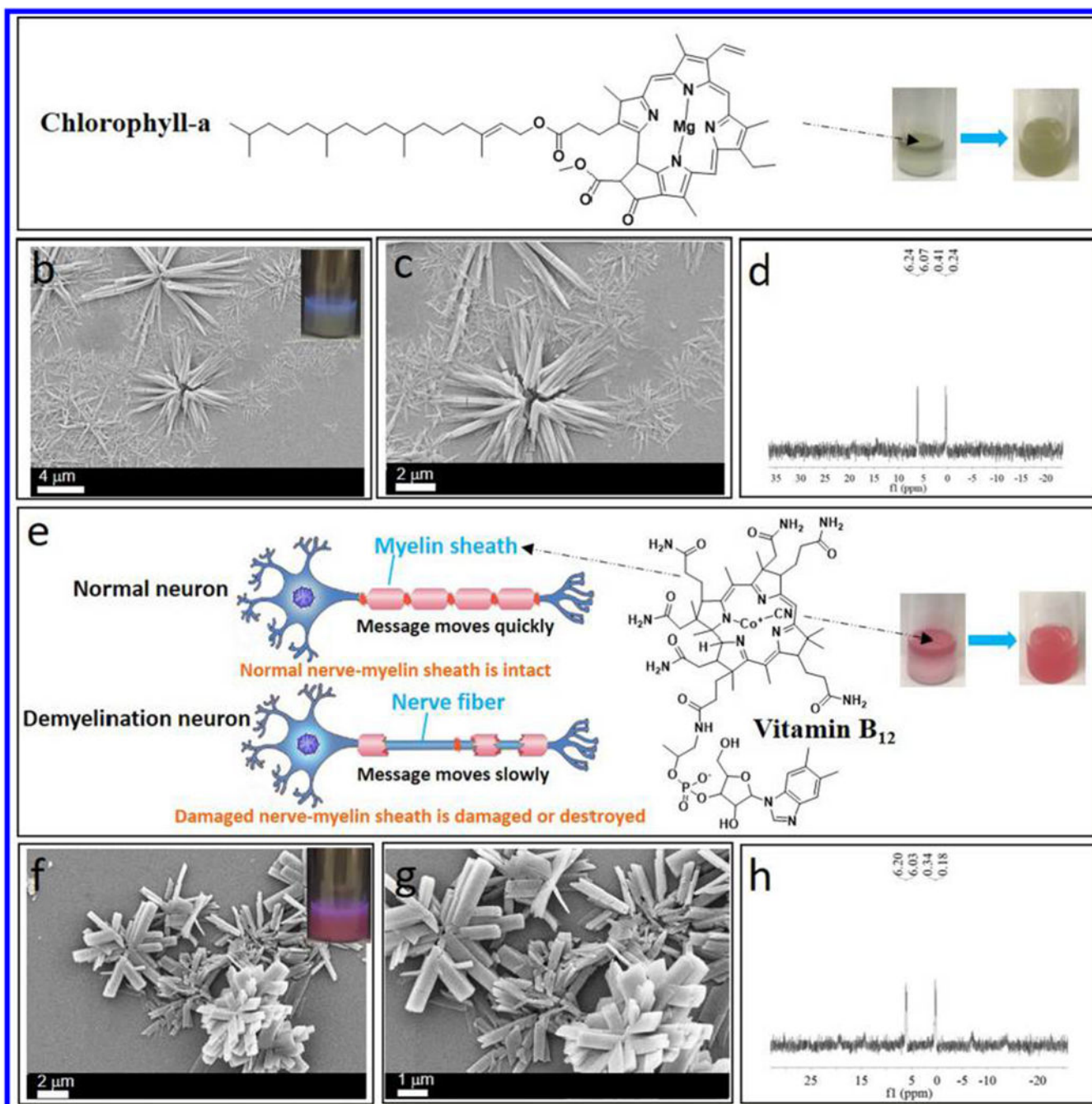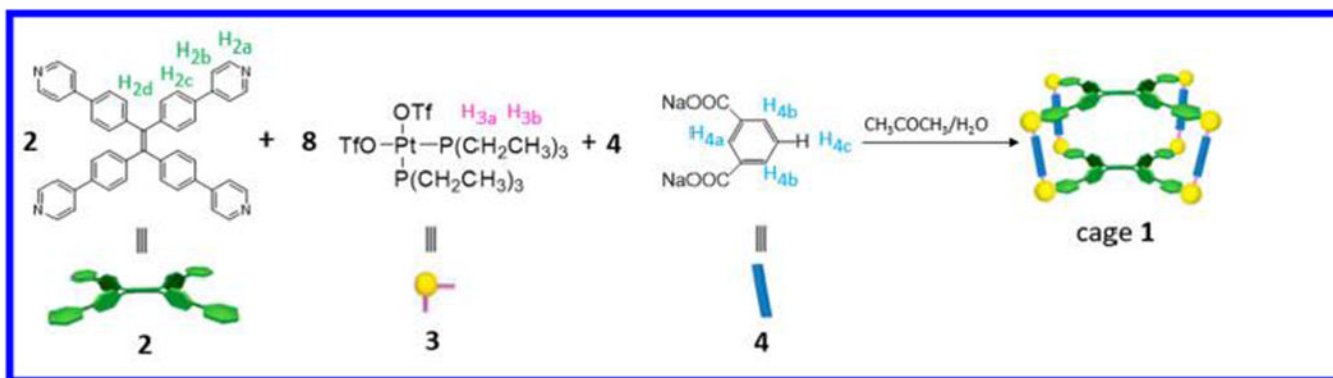
Figure 6.
(a) Chemical structure of Chl-a (right: optical image showing the "phase-transfer" co-assembly process). (b) SEM image of Chl-a-containing microflowers. (c) In situ SEM image at higher magnification. (d) $^{31}P\{^1H\}$ NMR spectra of Chl-a-containing microflowers redispersed in DCM. (e) Chemical structure of vitamin B$_{12}$ (right: optical image showing the "phase-transfer" co-assembly process). (f) SEM image of vitamin B$_{12}$-containing microflowers. (g) In situ SEM image at higher magnification. (h) $^{31}P\{^1H\}$ NMR spectra of vitamin B$_{12}$-containing microflowers redispersed in DCM.

Scheme 1.
[2+8+4] Assembly of 2, 3, and 4 To Furnish Cage 1

Scheme 2.
Proposed Mechanism of Formation of the Microflowers[a]

[a] Steps 1–4 show the formation of cage **1**-based microflowers, and steps 5–9 show the co-assembly of cage **1** and perylene-based microflowers. The inset shows the chemical structures corresponding to cage **1** and perylene. Black arrows in the bottom images indicate magnification of microflowers and microneedles.